

# Optimization and Assessment of the Comprehensive Performance of an Axial Separator by Response Surface Methodology

D. Z. Zhu<sup>1</sup>, D. Han<sup>1†</sup>, W. F. He<sup>1</sup>, J. J. Chen<sup>1</sup>, Y. Y. Ji<sup>1</sup>, T. Peng<sup>1,2</sup> and Y. W. Gu<sup>1</sup>

<sup>1</sup> College of Energy and Power Engineering, Nanjing University of Aeronautics and Astronautics I, Nanjing, Jiangsu, 210001, China

<sup>2</sup> Jiangsu Loke Energy Saving Technology Co, Ltd2, Taizhou, Jiangsu, 214500, China

†Corresponding author E-mail: [handong@nuaa.edu.cn](mailto:handong@nuaa.edu.cn)

(Received June 14, 2022; accepted August 17, 2022)

## ABSTRACT

The separator with inner channels is designed to solve the inefficiency caused by particle collisions with the wall. Then the response surface methodology is used to optimize this novel separator with the aim of maximizing the separation efficiency and exhaust rate while minimizing the pressure drop simultaneously. Firstly, the Reynolds Stress model and the Euler-Euler model are taken to compare the novel and conventional structures. Secondly, five factors, including inlet velocity ( $v$ ) of air-particle flow, number of inner channels, axial angle of inner channels, height of inner channels, and number of guide vanes, are selected in the Box-Behnken Design. Thirdly, the quadratic regression equations are established in multi-objective optimization. The research results demonstrate that separation efficiency is improved but the pressure drop is increased in the novel design. Additionally, too large inner channels can lead to a decrease in separation efficiency. The increased height of the inner channels has the most positive impact on the exhaust rate. And the optimization amplitude of the pressure drop is the most remarkable, which is presented as 13.87% at  $v = 2.5$  m/s, 34.49% at  $v = 4.5$  m/s, and 75.49% at  $v = 6.5$  m/s, respectively. Furthermore, the separation efficiency of optimized designs is higher than that of conventional ones at each velocity. The relevant research results can provide an effective guide for improving the efficiency of separators.

**Keywords:** Axial flow separator; Inner channel; Response surface; Multi-objective optimization; Separation efficiency.

## 1. INTRODUCTION

In the industrial field, cyclone separators are widely used in energy, chemical, and other industries to separate particles or droplets from airflow due to their simple structure, low cost, convenient maintenance, and no moving components (Kou and Wu 2020; Jin *et al.* 2019). Cyclone separators can be divided into tangential flow types and axial flow types according to the inlet mode, where the axial flow cyclone ones are applied successively because of their small pressure drop and convenient installation (Dziubak *et al.* 2020; Elsayed 2015). Generally, separation efficiency and pressure drop have always been important performance indicators for evaluating cyclone separators, which are directly related to the structure of the separator itself to a great extent (Mao *et al.* 2019). However, the reduction of separation efficiency caused by particle-wall collisions has always been a problem in separators (Li *et al.* 2020).

The influence of flow performance has been studied through experiments and computational fluid dynamics (CFD) in cyclone separators. Chen *et al.* (2021) found the tendency of efficiency in the different velocities and the distribution law of the flow field. With an increase in inlet velocity, the separation efficiency of waxing droplets of different particle sizes gradually increases. The static pressure is symmetrical along the centerline, and the radial pressure distribution is V-shaped, gradually increasing from the middle to both sides. Furthermore, the pressure loss increases from the increase in velocity, and the exhaust flows increase from the increase in the negative pressure at the exhaust outlet (Wu and Zhou 2018). Through large eddy simulation (LES) and experimental comparison, Francisco *et al.* (2012) noticed that turbulence plays an important role in particle movement. The turbulence can lead to particle re-entrainment, and the separation efficiency will be hindered. Simultaneously, the collection standard based on particles discharged via overflow is not applicable to cyclone separators without dust collectors. Elsayed

(2018) also concluded that the eccentricity provided by the turbulence to the eddy current detector significantly affects the performance of the cyclone separator. The curvature of the vortex core increased by 34.5% with the increase in eccentricity. And the above situation can be improved by adding new structures because the development of the vortex core can be limited, leading to a high separation efficiency (Karagoz *et al.* 2013). Additionally, setting up two-stage or three-stage separation is also an effective method to improve the performance of small cyclone separators (Souza *et al.* 2015; Venkatesh *et al.* 2021). The collection efficiency of the separators linked in series is higher than that of a single square cyclone, while the pressure drop is reduced to 14.3% by this series arrangement configuration (Venkatesh *et al.* 2021). And an increase in near gravity particles generates the turbulent accumulation of particles near the region just under the vortex finder, leading to the vortex finder overloading (Chen *et al.* 2017). Furthermore, collisions of particles of different sizes cause secondary particle breakage because the gas-particle coupling force and collision force are much larger than the particle gravity (Zhou *et al.* 2019).

Some researchers study the performance of the separator in special conditions. Under a magnetic field, the separation efficiency is very sensitive to the vertical distance of the magnetic source from the origin (Safikhani *et al.* 2020). Moreover, it provides higher efficiency by utilizing the preponderance of a magnetic field without imposing the pressure drop. And the influence of the magnetic field on particles with smaller diameters is more obvious than that on particles with bigger diameters. Besides, separation of the coarse and fine powder should be realized by different devices due to the complexity of the flow field under hypersonic conditions (Wu and Zhou 2018).

Simultaneously, algorithms (Luciano *et al.* 2018), response surfaces (Li *et al.* 2020), and other optimization methods are considered to optimize the structural and operational parameters of the separator to select suitable separation efficiency and pressure drop. A new grid independence check framework has been introduced which depends on the adjoint solver to locally refine the mesh for the minimum pressure drop. This method can optimize the local turbulent field (Elsayed 2015). The geometric structure of the separator is optimized using response surface methodology and a multi-objective genetic algorithm to obtain higher separation efficiency (Sun and Yoon 2018; Sun *et al.* 2017). To evaluate the collection performance of a cyclone, the use of "total efficiency" for the optimization of a cyclone using CFD is exceedingly reasonable, feasible, and convenient (Sun *et al.* 2017). And Zhao *et al.* (2020) applied the artificial neural network to establish the complex relationship between the pressure drop coefficient and the geometric size of the cyclone, where the guide vane is the key component of the axial cyclone separator. The separation efficiency is improved and the pressure drop is increased as the number and angle of the guide vanes are increased using multi-objective optimization. (Deng and Sun

2020). More guide vanes can give rise to an improvement in the separation efficiency, but the pressure drop is increased with the experiments and simulations (Xing *et al.* 2021). Meanwhile, the internal angle of the vane has a greater impact on the separation efficiency than the angle difference does. Furthermore, decreasing the inlet width and inlet height reduces the pressure drop and increases the collection efficiency via optimization (Venkatesh *et al.* 2020). Additionally, the separation efficiency is increased with the increase of the pitch, pipe length, and inlet velocity by combining the response surface method and genetic algorithm (Yang *et al.* 2019). Among them, the response surface method can be used to analyze efficiently and accurately the influence of single factor or multifactor interactions in separators. Because the calculation of this method is simple and fast, it is widely used (Sun *et al.* 2017; Deng and Sun 2020).

It is summarized that the re-entrainment phenomenon, in which the silica as the basic pollution is collided with wall, is a major issue in separators. Furthermore, it is one of the most important reasons for the decrease in separation efficiency. However, no separation device can achieve efficient separation of silica from the air due to this phenomenon. In this paper, a novel structure for the axial cyclone separator is designed with the inner channels to solve this problem. The multi-objective optimization of the novel design is considered based on the response surface method, with the inner channels and the guide vane as the factors. Then the Box-Behnken Design (BBD) is used to get the quadratic regression equations via CFD. After the interactions of factors are investigated by the response surfaces, the optimized parameters are calculated. Finally, the separation efficiency and pressure drop are compared between the conventional separator and optimized ones at each velocity. The characteristics of the separator with inner channels can provide effective guidance for mechanical dust removal.

## 2. MODELING AND NUMERICAL METHODS

### 2.1. Model Establishment

As shown in Fig. 1, the different designs are displayed. Among them, the axial angle of inner channels ( $\gamma$ ) and the height of inner channels ( $h$ ) are variable. The detailed dimensions of the separators are shown in Table 1, wherein the inner channels are the shell, and the thickness of these is negligible.

### 2.2. Mathematical Model

The Reynolds Stress model (RSM) is adopted to simulate the turbulent motion, while the Euler-Euler model is used to describe the air-particle flow (Zhou *et al.* 2019; Mao *et al.* 2019; Rocha *et al.* 2015; Wei and Gao 2020). In comparison to single-equation or two-equation models, the RSM includes the exact term of the vortex effect in the stress transport equation. It can capture the most physical phenomena since it is itself anisotropic, which means

it takes the influence of the vortex into account more closely and offers data on all stress components.

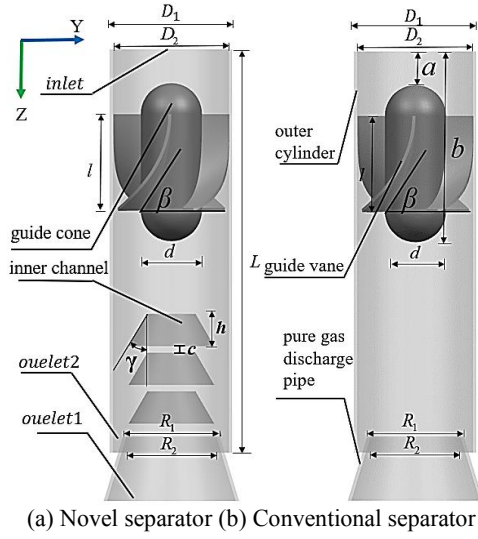


Fig. 1. Axial flow separator structure.

Table 1. Structural parameters of the separators

Parameter	Value
$D_1$ (outer diameter of the separator)	40 mm
$D_2$ (inner diameter of the separator)	36 mm
$d$ (the diameter of the guide cone)	18 mm
$l$ (length of the guide vane)	19 mm
$R_1$ (outer diameter of the pure gas discharge pipe)	30 mm
$R_2$ (inner diameter of the pure gas discharge pipe)	28 mm
$L$ (length of the outer cylinder)	125 mm
$a$ (distance from inlet to top of guide cone)	10.5 mm
$b$ (distance from inlet to bottom of guide cone)	59.5 mm
$c$ (distance between inner channel)	2 mm
$\beta$ (outlet angle of the guide vane)	60 °
$I$ (diameter of upper bottom of inner channel)	15 mm

For RSM, the following continuity equations and Reynolds-averaged Navier-Stokes (RANS) equations are used:

$$\frac{\partial \rho}{\partial t} + \frac{\partial}{\partial x_i} (\rho u_i) = 0, \quad (1)$$

$$\frac{\partial}{\partial t} (\rho u_i) + \frac{\partial}{\partial x_j} (\rho u_i u_j) = -\frac{\partial p}{\partial x_i} + \frac{\partial}{\partial x_j} (-\overline{\rho u_i u_j}) + \frac{\partial}{\partial x_j} \left[ \mu \left( \frac{\partial u_i}{\partial x_j} + \frac{\partial u_j}{\partial x_i} \right) \right], \quad (2)$$

where  $\rho$ ,  $u$ ,  $t$ ,  $p$  and  $\mu$  are air density, air velocity, time, fluid pressure, and the dynamic viscosity of air, respectively.  $-\overline{\rho u_i u_j}$  is Reynolds shear stress, which refers to the additional stress caused by pulsating momentum exchange with the Reynolds equation, including additional normal stress and shear stress, and subscripts  $i$  and  $j$  are components in the Cartesian coordinate system.

The Euler-Euler model, based on the Euler-Euler coordinated system, better describes the interaction between particles and fluids (Meier and Mori 1998). It mimics gas-solid two-phase flow as the most complicated multiphase flow model currently. When the particle phase is treated as a continuum, additional stress tensor and pressure terms appear in the momentum equation of this phase, and a suitable closure model is needed to close the equations. In this paper, the Kinetic Theory of Granular Flow (KTGF) is used to seal the two terms.

The continuity equation and the momentum equation in air flow are:

$$\frac{\partial}{\partial t} (\alpha_g \rho_g) + \nabla \cdot (\alpha_g \rho_g \mathbf{u}_g) = 0, \quad (3)$$

$$\frac{\partial}{\partial t} (\alpha_g \rho_g \mathbf{u}_g) + \nabla \cdot (\alpha_g \rho_g \mathbf{u}_g \mathbf{u}_g) = -\alpha_g \nabla p_g + \nabla \cdot \boldsymbol{\tau}_g - \beta (\mathbf{u}_g - \mathbf{u}_s) + \alpha_g \rho_g \mathbf{g}$$

where  $\alpha_g$  is the phase volume fraction of the air,  $\mathbf{u}_g$  is the velocity of the air,  $\mathbf{g}$  is the specific gravity force, and  $\boldsymbol{\tau}_g$  is the shear stress of the air.

The continuity equation and the momentum equation in particle flow are (Zhao and Zhong 2013):

$$\frac{\partial}{\partial t} (\alpha_s \rho_s) + \nabla \cdot (\alpha_s \rho_s \mathbf{u}_s) = 0, \quad (5)$$

$$\frac{\partial}{\partial t} (\alpha_s \rho_s \mathbf{u}_s) + \nabla \cdot (\alpha_s \rho_s \mathbf{u}_s \mathbf{u}_s) = -\alpha_s \nabla p_g + \nabla \cdot \boldsymbol{\tau}_s + \beta (\mathbf{u}_g - \mathbf{u}_s) + \alpha_s \rho_s \mathbf{g}$$

where  $\alpha_s$  is the phase volume fraction of the particle,  $\mathbf{u}_s$  is the velocity of the particle,  $\mathbf{g}$  is the specific

gravity force, and  $\boldsymbol{\tau}_s$  is the shear stress of the air.

The shear stress of air is expressed as follows:

$$\boldsymbol{\tau}_g = \alpha_g \mu_{g,\text{eff}} [\nabla \mathbf{u}_g + (\nabla \mathbf{u}_g)^T] + \alpha_g \left( \lambda_g - \frac{2}{3} \mu_{g,\text{eff}} \right) (\nabla \cdot \mathbf{u}_g) \mathbf{I} \quad (7)$$

where  $\mu_{g,\text{eff}}$  is the effective viscosity.

Here  $\beta$  is the drag coefficient of air-particle flow, defined as:

$$\beta = \begin{cases} \frac{3}{4} C_D \frac{\alpha_s \alpha_g \rho_g |\mathbf{u}_g - \mathbf{u}_s|}{d_s} \alpha_g^{-2.65} & \alpha_g > 0.8 \\ 150 \frac{\alpha_s^2 \mu_g}{\alpha_g d_s^2} + 1.75 \frac{\rho_g \alpha_s}{d_s} & \alpha_g \leq 0.8 \end{cases}, \quad (8)$$

$$C_D = \begin{cases} \frac{24}{Re_s} [1 + 0.15(Re_s)^{0.687}] & Re_s < 1000 \\ 0.44 & Re_s \geq 1000 \end{cases}, \quad (9)$$

$$Re_s = \frac{\alpha_g \rho_g d_s |\mathbf{u}_s - \mathbf{u}_g|}{\mu_g}, \quad (10)$$

The particle temperature is expressed as:

$$\Theta_s = \frac{1}{3} (\mathbf{u}_s^2), \quad (11)$$

The particle phase pressure equation is expressed as:

$$P_s = \alpha_s \rho_s \Theta_s + 2 \rho_s (1 + e_{ss}) \alpha_s^2 g_{0,ss} \Theta_s, \quad (12)$$

where  $e_{ss}$  is the particle-particle collision restitution coefficient.

The radial distribution function is expressed as:

$$g_{0,ss} = \left[ 1 - \left( \frac{\alpha_s}{\alpha_{s,\text{max}}} \right)^{1/3} \right]^{-1}, \quad (13)$$

The energy transfer equation is expressed as:

$$\varphi_{gs} = -3\beta \cdot \Theta_s, \quad (14)$$

In numerical simulation, the separation efficiency can be calculated as:

$$\varphi = \frac{q_{\text{outlet2,particles}}}{q_{\text{inlet,particles}}}, \quad (15)$$

where  $q_{\text{outlet2,particles}}$  is the mass flow of particles from the outlet 2 and  $q_{\text{inlet,particles}}$  is the mass flow of particles from the inlet.

### 2.3. Simulation Method

The conditions are shown in Table 2. The velocity inlet boundary condition is taken at the inlet, while the pressure outlet is chosen as the outlet boundary condition. The inlet velocity of silica as the particle phase is identical to that of air as the continuous

phase. And the interaction of the particle phase on the continuous phase is ignored because of the small volume fraction of particles. Besides, the Euler-Euler model using Gidaspow as the drag model is applied to solve air-particle flows (Meier 1998; Xing *et al.* 2021).

The SIMPLEC algorithm is utilized in pressure-velocity coupling, and the Presto! interpolation method is suitable for pressure. The QUICK method is used to solve the turbulent dissipation rate. And then the first-order upwind scheme is taken for momentum and turbulent kinetic energy.

**Table 2. Parameters of air-particle flow**

	Parameters	Value
Air flow	Inlet velocity	2.5, 4.5, 6.5 m/s
	Density	1.225 kg/m <sup>3</sup>
	Turbulent intensity	5%
	Kinematic viscosity	2.0 × 10 <sup>5</sup> kg/m·s
Particle flow	Inlet velocity	2.5, 4.5, 6.5 m/s
	Density	2650 kg/m <sup>3</sup>
	Volume fraction	0.001
	Diameter	20-40 um

### 2.4. Grids Verification and Model Validation

As shown in Fig. 2, hexahedral grids are provided because they have higher accuracy and require fewer computing resources to describe precisely the flow in the separator. Moreover, the flow field inside the separator is simulated by using Fluent after the grids are divided by using icem19.2.

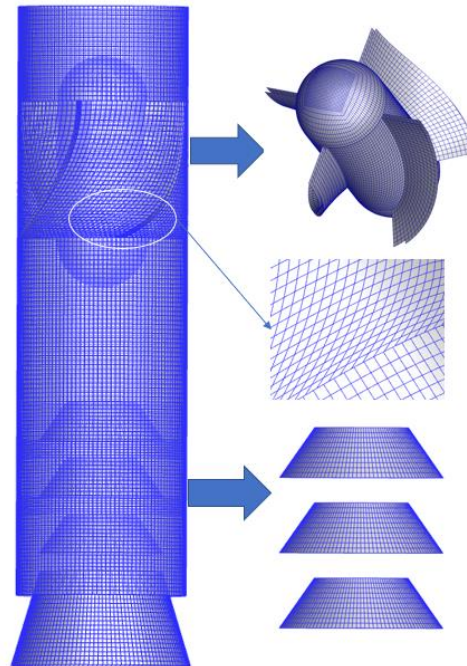


**Fig. 2. Grid division of separator.**

As shown in Fig. 3, grid refinement ratio is 1.2, and the front end and rear end of the guide vane were locally dense to ensure the accuracy of the cyclone calculation. And hexahedral grids of the numbers 227300, 366141, 585367, and 1362342 are established, respectively. The pressure and velocity of outlet1 are compared in the different grids. The number of 585367 and 1362342 hexahedral grids is almost identical in the separators. As can be seen, the pressure changes by about 10.34%, 3.64%, and 0.97%, respectively, and the velocity changes by about 16.26%, 10.76%, and 0.98%, respectively. Therefore, a numerical model is proposed to save computational resources and time with about the number of 585367 hexahedral grids.

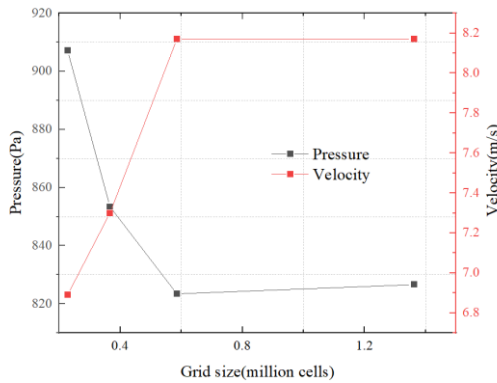


Fig. 3. Grid independence verification.

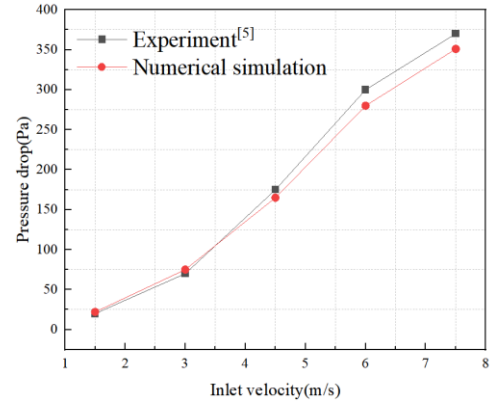
To verify the simulated results, it is necessary to compare the prediction with experimental data. To do this, we compared the simulated results to previously published experimental results by *Mao et al.* (2019). Inlet velocities are measured at 1.5, 3, 4.5, 6, and 7.5 m/s, respectively. Similarly, particle sizes of 75  $\mu\text{m}$ , 120  $\mu\text{m}$ , 150  $\mu\text{m}$ , 180  $\mu\text{m}$ , 250  $\mu\text{m}$ , and 270  $\mu\text{m}$  were selected to verify the separation efficiency when the velocity is 5 m/s. The velocity inlet and pressure outlet for particles that are the same as air are adopted corresponding to the experimental conditions.

Figure 4 shows that the simulation results are almost in agreement with the experimental results. The largest deviations in the pressure drop and efficiency are 5.13% and 4.41%, respectively, denoting that the RSM and the Euler-Euler model can predict the pressure drop and efficiency of the separator precisely.

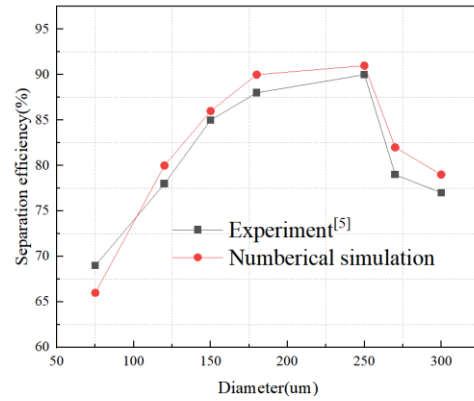
### 3. DESIGN OF RESPONSE SURFACES

To explore the influence of inner channels on performance parameters, response surface methodology is applied to obtain the interaction among factors to optimize performance parameters (*Gao et al.* 2020). In the practical application process, high efficiency and low pressure drop are considered in the separator. And the exhaust rate herein is also taken as the optimization goal because the new design has a great impact on it. The optimization design steps include variance analysis, response

surface analysis, and quadratic regression equation optimization.



(a) Validation of the pressure drop



(b) Validation of the separation efficiency

Fig. 4. Comparison of experimental and simulation results.

The main purpose of this optimization is to evaluate the separation efficiency, pressure drop, and exhaust rate of the novel axial flow separator, where the exhaust rate is defined as:

$$\delta = \frac{q_{outlet,air}}{q_{inlet,air}}, \quad (16)$$

where  $q_{outlet,air}$  is the air flow from the outlet1 and  $q_{in,air}$  is the air flow from the inlet.

Response surface methodology optimizes multivariable problems by fitting the functional relationship between independent variables and the response index (*Tag and Yanik* 2018), which is generally realized by a second-order polynomial model, namely:

$$y = e_0 + \sum_{i=1}^n e_i x_i + \sum_{i=1}^n \sum_{j=i+1}^n e_{ij} x_i x_j + \sum_{i=1}^n e_{ii} x_i^2 + b, \quad (17)$$

where  $y$  is the system response index, and  $e$  is the regression coefficient of linear, quadratic, truncated, and their interactions. Moreover,  $x_i$  and  $x_j$  are independent variables,  $b$  is the statistical error, and  $n$

is the number of variables.

In response surface methodology, Box-Behnken Design (BBD) and Central Composite Design (CCD) are generally included in Design-Expert 13, from which BBD is adapted. Inlet velocity ( $v$ ) is considered because it has a significant influence on separation efficiency and pressure drop. Similarly, structural parameters such as the number of inner channels ( $n$ ), axial angle of inner channels ( $\gamma$ ), and height of inner channels ( $h$ ) are selected to study their influence on separator performance. Installation positions for inner channels range from  $z=60$  mm to  $z=116$  mm. The number of guiding vanes ( $m$ ) is adopted as one of the design factors in this work to make the distribution of flow parameters more uniform and reasonable. The specific parameters are designed in Table 3, and the responses are decided in Table 4. Especially, the factors, including  $v$ ,  $n$ ,  $\gamma$ ,  $h$ ,  $m$ , are used as the design variables, and responses are opted as objective functions.

#### 4. MULTI-OBJECTIVE OPTIMIZATION

##### 4.1. BBD Scheme

The response indices are separation efficiency, pressure drop, and exhaust rate in BBD, and an optimization scheme is selected to generate 46 groups of samples via CFD. The results are shown in Table 5. Among them, the separation efficiency is relatively high and the change in it is relatively small. This is because the inner channels prevent the re-entrainment of particles.

##### 4.2. Quadratic regression equation model and diagnosis

In the experimental scheme, the modified separation efficiency equation is described as follows:

$$\begin{aligned} \varphi = & -7.84049 - 5.05969*v + 15.85313*n \\ & + 4.66124*\gamma + 5.32656*h - 4.76469*m \\ & + 0.695*v*n + 0.229375*v*h \\ & - 0.3065*n*\gamma - 0.785*n*h \\ & - 0.154472*\gamma*h + 0.385*h*m \\ & - 0.033407*\gamma^2 \end{aligned} \quad (18)$$

Similarly, the modified pressure drop equation is described as follows:

$$\begin{aligned} \Delta P = & 16570.74586 - 788.56851*v - 291.66256*n \\ & - 553.72645*\gamma - 1198.45953*h \\ & + 19.45475*m + 13.5517*v*\gamma \\ & + 33.41384*v*h + 9.09771*n*\gamma \\ & + 18.91692*\gamma*h + 11.16356*v^2 \\ & + 4.46661*\gamma^2 + 24.16661*h^2 \end{aligned} \quad (19)$$

The modified exhaust rate is represented as follows:

$$\begin{aligned} \delta = & 430.24156 + 0.711875*v \\ & - 24.71045*n - 12.33404*\gamma \\ & - 33.13578*h + 0.9165*n*\gamma \\ & + 0.714562*\gamma*h - 1.42128*n^2 \\ & + 0.06269*\gamma^2 + 0.607232*h^2 \end{aligned} \quad (20)$$

The sum of squares of each item in the model is adopted to evaluate the fluctuation of experimental data, while the mean square error is the estimation of the variance term. The F value compares the mean square of each item with the residual error to test the accuracy of the model, and the P value is taken to evaluate whether the experiment is significant. If the value of P is less than 0.05, it proves that the data is available (Gao *et al.* 2020). Besides, Adeq Precision is the signal-to-noise ratio, and a ratio greater than 4 is desirable.

Table 3. Factors of BBD model

Factor	Unit	Low value	Middle value	High value
$v$	m/s	2.5	4.5	6.5
$n$		2	3	4
$\gamma$	°	30	35	40
$h$	mm	8	10	12
$m$		4	6	8

Table 4. Responses of BBD model

Response	Unit	Goal
Separation efficiency ( $\varphi$ )	%	maximize
Pressure drop ( $\Delta P$ )	Pa	minimize
Exhaust rate ( $\delta$ )	%	maximize

According to BBD, the variance results of separation efficiency, pressure drop, and exhaust rate are shown in Table 6, and it means the models established by each response function are suitable for the test scheme.

##### 4.3. Influences on Separation Efficiency

Figure 5 shows the response surface between the number and angle of the inner channels on separation efficiency. It is found that the separation efficiency does not increase with the increase in the number and the axial angle of inner channels. When they are too large, they will also have a negative impact on the separation efficiency. The size of inner channels can facilitate turbulent fluctuation, in which the flow of particles is more chaotic. This causes some particles to be unseparated.

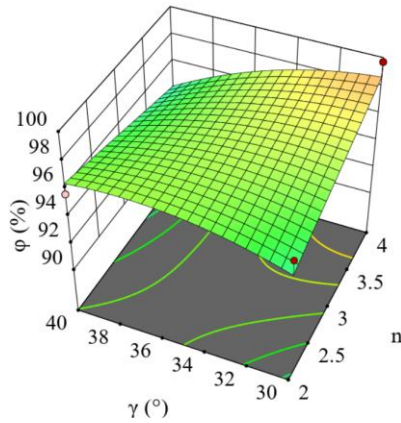
Figure 6 shows vividly the influence of the height of the inner channels and the number of the guide vanes. The response surface illustrates that the separation efficiency can be improved as the height of the inner channels and the number of guide vanes are increased. The reason is that the greater the number of guide vanes, the more uniform the velocity distribution, the better the cyclone effect. And the re-entrainment of particles can be more effectively inhibited if the height of inner channels is improved. This can prevent particles from entering the compression vortex.

**Table 5 BBD simulation schemes**

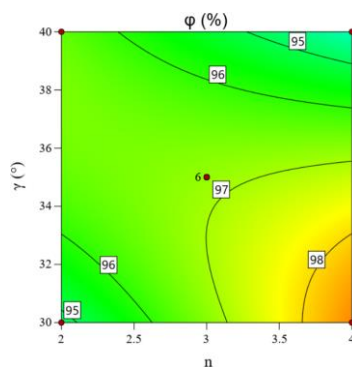
Sample	$v$ (m/s)	$n$	$\gamma$ (°)	$h$ (mm)	$m$	$\varphi$ (%)	$\Delta P$ (Pa)	$\delta$ (%)
1	4.5	3	40	10	8	92.81	559.80	83.46
2	2.5	3	40	10	6	97.55	142.24	81.15
3	6.5	2	35	10	6	93.50	454.90	70.13
4	4.5	4	40	10	6	93.39	565.22	85.23
5	4.5	3	35	8	4	97.40	133.10	65.14
6	2.5	4	35	10	6	97.80	71.69	70.05
7	4.5	3	30	12	6	99.71	377.70	66.52
8	2.5	3	35	10	8	97.84	86.48	71.20
9	4.5	2	35	10	4	98.30	193.29	69.02
10	4.5	3	35	10	6	96.74	247.81	72.9
11	4.5	3	35	10	6	96.74	247.81	72.9
12	2.5	3	35	8	6	96.8	49.14	63.19
13	4.5	3	40	10	4	98.17	401.95	79.55
14	4.5	3	35	8	8	91.56	183.93	67.00
15	2.5	3	35	12	6	99.25	134.18	81.08
16	4.5	3	35	10	6	96.74	247.81	72.9
17	4.5	4	35	12	6	95.05	498.16	80.83
18	4.5	3	40	8	6	94.37	220.64	71.56
19	4.5	3	35	10	6	96.74	247.81	72.90
20	6.5	3	30	10	6	95.67	332.08	67.90
21	6.5	3	35	12	6	99.27	941.90	82.9
22	6.5	3	35	10	4	97.44	430.65	70.67
23	4.5	3	35	10	6	96.74	247.81	72.90
24	4.5	4	35	10	4	99.75	217.43	69.12
25	4.5	3	35	12	4	98.46	393.98	80.43
26	6.5	3	40	10	6	94.95	965.13	84.30
27	2.5	3	30	10	6	98.62	51.25	63.76
28	4.5	3	35	12	8	98.78	504.90	83.85
29	4.5	2	35	12	6	99.75	388.91	84.16
30	4.5	4	35	8	6	96.40	161.82	65.50
31	4.5	3	30	10	4	98.24	137.81	64.87
32	4.5	3	40	12	6	95.66	1224.77	66.65
33	4.5	2	35	8	6	94.82	148.96	66.08
34	6.5	3	35	10	8	92.77	556.91	74.74
35	4.5	2	35	10	8	93.65	249.95	74.60
36	4.5	3	30	10	8	93.70	190.26	66.97
37	4.5	3	30	8	6	92.32	130.24	65.64
38	4.5	3	35	10	6	96.74	247.81	72.90
39	4.5	2	40	10	6	95.67	372.77	83.03
40	6.5	3	35	8	6	93.15	322.24	68.09
41	2.5	3	35	10	4	99.60	64.93	68.46
42	4.5	4	35	10	8	96.98	264.76	70.91
43	6.5	4	35	10	6	97.89	517.01	71.69
44	4.5	2	30	10	6	95.85	156.10	66.91
45	2.5	2	35	10	6	98.97	69.67	68.75
46	4.5	4	30	10	6	99.70	166.59	50.78

**Table 6 Variance results**

	Sum of squares	Mean square deviation	F-value	P-value	Adeq Precision
$\varphi$	202.18	16.85	17.67	<0.0001	16.0322
$\Delta P$	$2.580 \times 10^6$	$2.150 \times 10^5$	47.97	<0.0001	28.3426
$\delta$	2247.32	224.73	60.87	<0.0001	30.1683

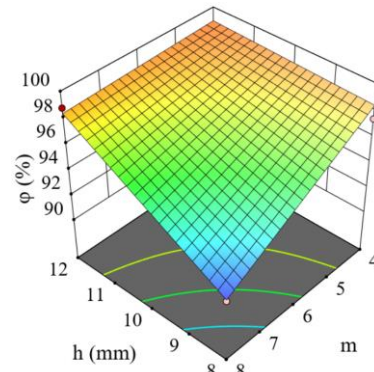


(a) 3D response surface plot

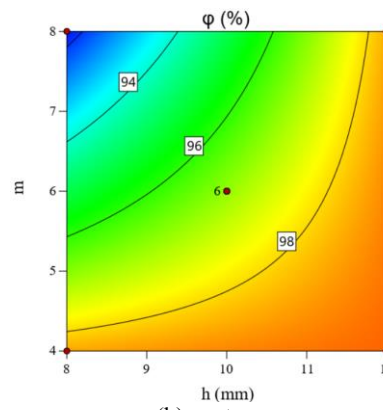


(b) contour

**Fig. 5. Response surface between the number and angle of inner channels on separation efficiency.**



(a) 3D response surface plot



(b) contour

**Fig. 6. Response surface between the height of inner channels and number of guide vanes on separation efficiency.**

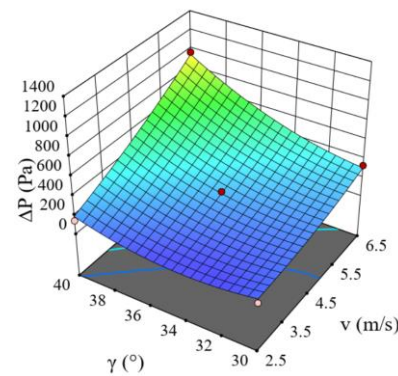
#### 4.4. Influences on Pressure Drop

The response surface is shown in Fig. 7 between the axial angle of the inner channels and the velocity on pressure drop. It can be clearly seen that the pressure drop increases with the increase of these factors. When the interaction of the two factors is described, the pressure drop increases rapidly. Because the angle of the inner channels becomes larger, the work done by the fluid to overcome the resistance also becomes larger and the local loss increases.

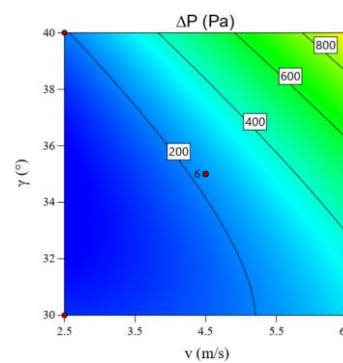
Figure 8 shows the response surfaces between the influence of the height and axial angle of inner channels on pressure drop. It is found that the axial angle and height of inner channels increased, leading to the pressure drop increasing. And the interaction of the two factors makes the pressure drop increase rapidly. The reason for this phenomenon is that the interaction of these factors can make the conversion of pressure energy into kinetic energy more violent. Additionally, the larger height and axial angle of inner channels can produce greater viscous shear stress, increasing the local resistance and the loss along the path.

#### 4.5. Influences on Exhaust Rate

From the response surface between the angle and height of inner channels on exhaust rate in Fig. 9, between the angle and number of inner channels on exhaust rate in Fig. 10. It can be seen that increases in exhaust rate are evident with the increase in the

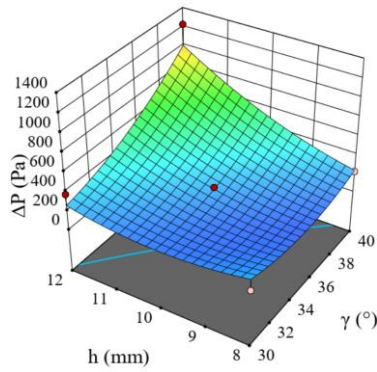


(a) 3D response surface plot

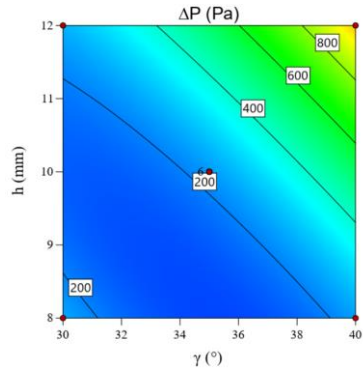


(b) contour

**Fig. 7. Response surface between the angle and velocity of inner channels on pressure drop.**

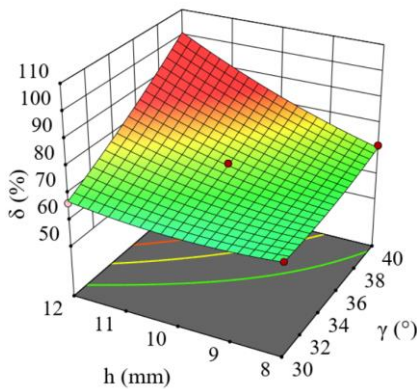


(a) 3D response surface plot

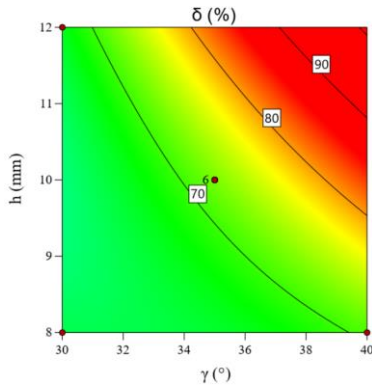


(b) contour

**Fig. 8. Response surface between the height and angle of inner channels on pressure drop.**



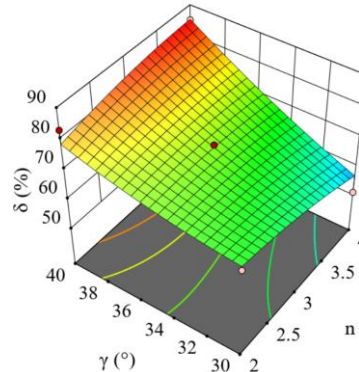
(a) 3D response surface plot



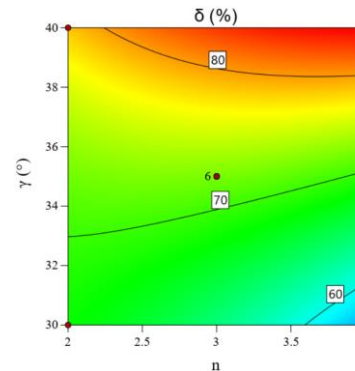
(b) contour

**Fig. 9. Response surface between the angle and height of inner channels on exhaust rate.**

size of inner channels. Simultaneously, the interaction between the height and axial angle of inner channels is greater than that between the height and the number of inner channels. Therefore, the exhaust rate is the most affected by the height of the inner channels. This is because fluid in the central flow field region is blocked from entering the near wall region due to the increase in the height of inner channels. And the air escapes the pure gas discharge pipe.



(a) 3D response surface plot



(b) contour

**Fig. 10. Response surface between the angle and number of inner channels on exhaust rate.**

#### 4.6. Optimization Results

Table 7 shows a comparison of samples at different velocities by CFD, and the comparison samples are samples 41, 24, and 21 before optimization at each velocity. And finally, the results show that the separation efficiency after multi-objective optimization has little change, while the pressure drop and exhaust rate have great change. The optimization of multi-objective factors mainly focuses on the height of the inner channel. When  $h$  decreases, the performance of the exhaust rate gets worse, but the pressure drop is reduced. For samples with velocities of 2.5, 4.5, and 6.5 m/s, the pressure drop decreases by 13.87%, 34.49%, and 75.49%, respectively. The effect of the pressure drop optimization is most obvious. This is because the structure size of the optimized inner channels always tends to decrease at different velocities, leading to the diminution of the resistance. Besides, the results of CFD and RSM are shown in Table 8. They are approximate, demonstrating that results can be used to compare the samples via CFD.

**Table 7 Results before and after multi-objective optimization by CFD**

Run.		$v$ (m/s)	$n$	$\gamma$ ( $^{\circ}$ )	$h$ (mm)	$m$	$\varphi$ (%)	$\Delta P$ (Pa)	$\mathcal{D}$ (%)
1	Before	2.5	3	35	10	4	99.6	64.93	68.46
2	After	2.5	2	35	11.17	4	99.98 ( $\uparrow$ 0.40%)	55.92 ( $\downarrow$ 13.87%)	71.82 ( $\uparrow$ 4.90%)
3	Before	4.5	4	35	10	4	99.75	217.43	69.12
4	After	4.5	4	35	8.59	4	99.84 ( $\uparrow$ 0.09%)	142.43 ( $\downarrow$ 34.49%)	64.68 ( $\downarrow$ 6.43%)
5	Before	6.5	3	35	12	6	99.27	941.90	82.9
6	After	6.5	4	30	9.11	4	98.87 ( $\downarrow$ 0.40%)	230.83 ( $\downarrow$ 75.49%)	62.50 ( $\downarrow$ 24.61%)

**Table 8 Simulation and RSM results after optimization**

Run.	$\varphi$ (%)			$\Delta P$ (Pa)			$\mathcal{D}$ (%)		
	CFD	RSM	Deviation	CFD	RSM	Deviation	CFD	RSM	Deviation
2	99.98	100	0.02%	55.92	54.56	2.49%	71.82	74.35	3.40%
4	99.84	100	0.16%	142.43	136.24	4.54%	64.68	63.46	1.92%
6	98.87	100	1.13%	230.83	216.76	7.35%	62.50	58.67	6.53%

Figure 11 shows the comparison between the optimized separator and conventional ones. The separation efficiency of optimized separators is higher than that of conventional ones at different velocities. This can prove that the novel separator has better performance after optimization because this phenomenon of re-entrainment is suppressed in these separators. And the pressure drop in the novel structure is increased due to the increased airflow resistance of the built-in structure. Moreover, the viscosity generates a large velocity gradient near the inner channel wall, forming a strong eddy motion. This will cause the pressure drop to go up because of the loss of energy. However, the pressure drop in the separators with the inner channels decreases after optimization. Besides, there is a slight difference in the exhaust rate in these separators.

## 5. RESULTS AND DISCUSSION

### 5.1. Particle Motion

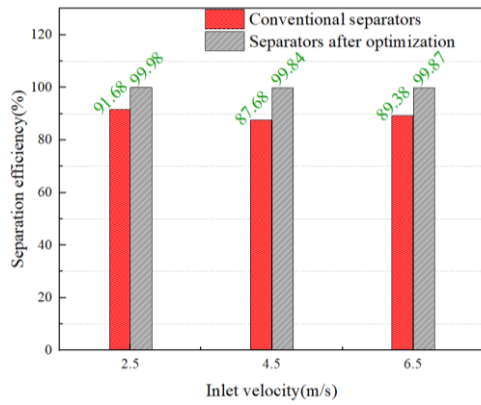
Figure 12 shows the volume fraction of particles between the novel after optimization and conventional structures at  $v=4.5$  m/s. After the guide vane, the particles are separated and bounce back by hitting the wall. Obviously, fewer particles enter the pure gas discharge pipe in the novel structure. This is because the inner channels block particles that produce elastic collisions from entering the central

flow field.

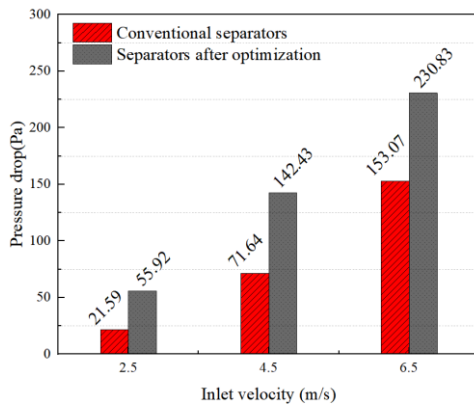
### 5.2. Influences on Pressure

Figure 13 shows the pressure field contours of separators with different structures. It is obvious that the pressure distributions of both the novel and conventional designs almost accord with the U-shaped symmetry. The pressure is almost symmetrical around the centerline of them. As the fluid flows through the guide vanes, expansion generates a large pressure drop, and there's a pressure gradient. The reason is that the pressure is converted into kinetic energy. Besides, there appears to be negative pressure after the guide vanes because the boundary layer separation happened on the side of the guide vanes. In the outer layer of the boundary layer separation zone, the phenomenon of turbulent diffusion is enhanced. This makes the particles move closer to the wall. While backflow occurs in the inner layer, the energy generation and dissipation of turbulence are low.

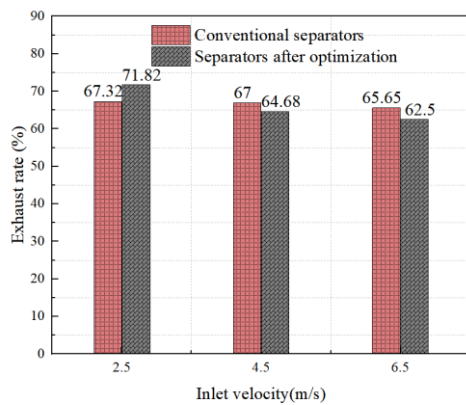
However, the novel structure has a large radial differential pressure after the guide vanes. This will lead to an increase in the pressure gradient force. Particles collide with the wall in the high-pressure region, and some particles escape to the low-pressure region after the collision. And the pressure decays seriously after the fluid flows through the inner channels that are gradually expanding. The cause can



(a) Separation efficiency of the separators



(b) Pressure drop of the separators



(c) Exhaust rate of the separators

**Fig. 11. Comparison of the separators.**

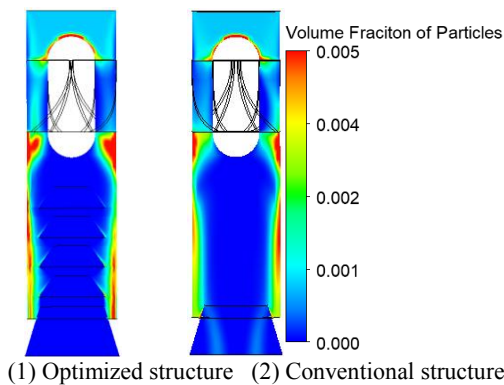


**Fig. 12. Volume fraction of particles.**

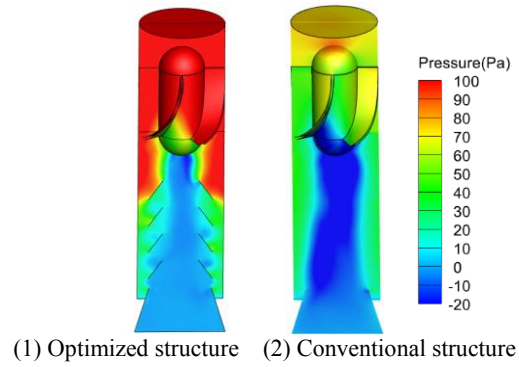


**Fig. 13. Pressure field contours of two separators.**

be traced to the inner channels that obstruct flow and increase local resistance. The flow between the outer cylinder and the inner channels is constricted, which lowers the pressure energy. But inner channels can also stop the deflection of the internal quasi-compression vortex in the Rankine vortex (Jeong and Hussain 1995). This effect can prevent the particles near the wall from entering the central flow field.

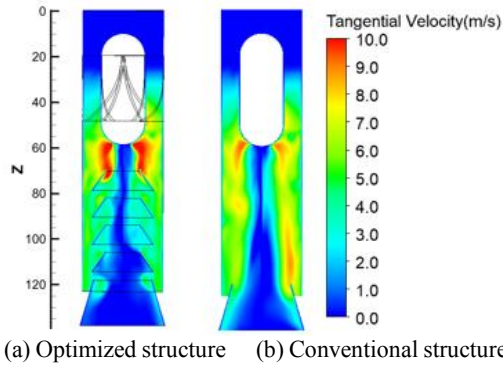
### 5.3. Influences on Tangential Velocity

Figure 14 shows the tangential velocity contour of the different structures. Tangential velocity appears when flowing through the guide vanes. And a large space of separation is formed on account of it. Simultaneously, tangential velocity increases before flowing through the inner channels in the novel structure. As shown in Fig. 15, the tangential velocity of the novel separator is greater than that of the conventional one at  $z_1=60$  mm, which can improve the separation efficiency, but no longer presents an axisymmetric bimodal distribution after passing through inner channels at  $z_2=117$  mm. Moreover, the increment of tangential velocity near the wall is too small in the novel separator at  $z_2=117$  mm. In short, the swirling flow is promoted in the first half and suppressed in the second half. This causes particles to be pre-rotated closer to the wall in the first half and cleaned up into the pure gas discharged in the second half.

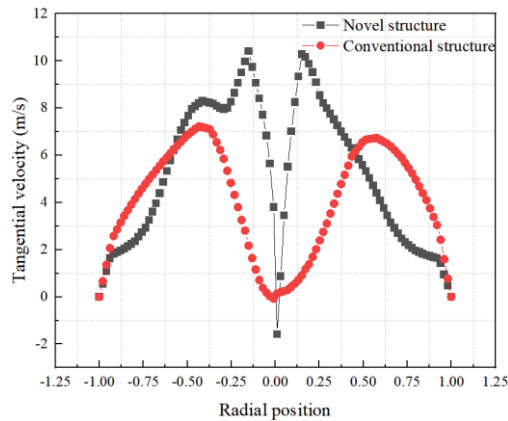
In the novel separator, the tangential velocity has improved at  $z_1=60$  mm, which is advantageous for separations of particles. There's a smaller momentum exchange between the molecules with low velocities and the ones with high velocities in different fluid layers. Then the resistance of the inner channels decreases the viscous stress between fluid layers, thereby the viscous transport work diminishes along the axial direction. This phenomenon changes the spatial distribution of energy, which increases the circumferential momentum.

## 1. CONCLUSIONS

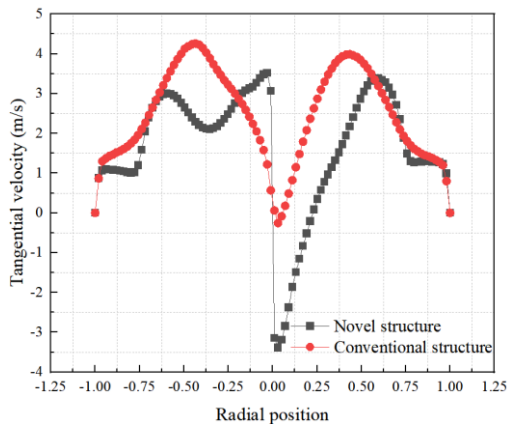
The axial flow separator with inner channels is studied, and the RSM and the Euler-Euler model are applied to predict the air-particle flow. The similarities and differences in internal flow fields are compared between the novel and conventional



**Fig. 14. Tangential velocity contour.**



(a)  $z_1=60$  mm



(b)  $z_2=117$  mm

**Fig. 15. Radial distribution of tangential velocity at  $z=60, 117$  mm.**

structures. Simultaneously, the reliability of the experimental optimization design is verified via CFD once the established regression models are utilized to describe the separation efficiency, pressure drop, and exhaust rate in the response surface methodology. From the results, the following conclusions are drawn:

[1] Inner channels can improve separation efficiency because the re-entrainment phenomenon of particles is prevented. In the novel separator, the tangential velocity is promoted after the guide vanes and before the inner channels, while the radial pressure is also

increased.

- [2] According to response surfaces, there is a maximum separation efficiency because inner channels that are too large can have an enlargement of the turbulent fluctuations. When these factors interact, the pressure drop increases rapidly. This is attributed to the work that becomes larger to overcome the resistance and the local loss with an increase in the size of the inner channels.
- [3] The optimization amplitude of the pressure drop is presented as 13.87% at  $v = 2.5$  m/s, 34.49% at  $v = 4.5$  m/s, and 75.49% at  $v = 6.5$  m/s, respectively, which shows the most obvious optimization effect. And the exhaust rate is most significantly affected by the increased height of the inner channels.
- [4] The optimized designs with the inner channels have a higher separation efficiency and pressure drop compared with conventional ones at every velocity. These characteristics make the novel separators have strong practical significance in the field of industrial dust removal.

#### ACKNOWLEDGEMENT

The authors acknowledge financial support from Postgraduate Research & Practice Innovation Program of NUAA (Grant NO. cxcxjh20210202).

#### REFERENCES

- Chen, J. Y. and Y. Zhang (2021). The use of axial cyclone separator in the separation of wax from natural gas: A theoretical approach, *Energy Reports* 7,2615-2624.
- Chen, K. C., R. Zou, A. B. Yu, A. Vince, G. D. Barnett and P. J. Barnett (2017). Systematic study of the effect of particle density distribution on the flow and performance of a dense medium cyclone, *Powder Technology* 314, 510-523.
- Deng, B. Y. and D. Sun (2020). Multi-objective optimization of guide vanes for axial flow cyclone using CFD, SVM, and NSGA II algorithm, *Powder Technology* 373, 637-646.
- Dziubak, L. B., M. Karczewski and M. Tomaszewski (2020). Numerical research on vortex tube separator for special vehicle engine inlet air filter, *Separation and Purification Technology* 2020 237, 116463.
- Elsayed, K. (2015). Design of a novel gas cyclone vortex finder using the adjoint method, *Separation and Purification Technology* 142, 274-286.
- Elsayed, B. K. (2018). Analysis and optimization of cyclone separators with eccentric vortex finders using large eddy simulation and artificial neural network, *Separation and Purification Technology* 207, 269-283.

- Gao, G., Z. Liu, B. Sun, D. Che and S. Li (2020). Multi-objective optimization of thermal performance of packed bed latent heat thermal storage system based on response surface method, *Renewable Energy* 153, 669-680.
- Jeong, F. H. (1995). On the identification of a vortex, *Journal of Fluid Mechanics* 285, 69-94.
- Jin, E. K., K. Dong, S. Dong, B. Wang, K. Kwok and M. Zhao (2020). Numerical study on the effect of the supersaturated vapor on the performance of a gas cyclone, *Powder Technology* 366,324-336.
- Karagoz, A. A., A. Surmen and O. Sendogan (2013). Design and performance evaluation of a new cyclone separator, *Journal of Aerosol Science* 59, 57-69.
- Kou, Y. C. and J. Wu (2020). Numerical study and optimization of liquid-liquid flow in cyclone pipe, *Chemical Engineering & Processing: Process Intensification* 147,107725.
- Li, T. W., L. Zhang, J. Chang, Z. Song and C. Ma (2020). Multi-objective optimization of axial-flow-type gas-particle cyclone separator using response surface methodology and computational fluid dynamics, *Atmospheric Pollution Research* 11, 1487-1499.
- Luciano, B. L. Silva, L. M. Rosa and H. F. Meier (2018). Multi-objective optimization of cyclone separators in series based on computational fluid dynamics, *Powder Technology* 325, 452-466.
- Mao, W. P., Hao Z., Q. Zhang, Z. Song, K. Chen and D. Han (2019). Orthogonal experimental design of an axial flow cyclone separator, *Chemical Engineering & Processing: Process Intensification* 144, 107645.
- Meier, M. M. (1998). Gas-solid flow in cyclones: The Eulerian-Eulerian approach, *Computers & Chemical Engineering* 22, 641-644.
- Rocha, A. C. Bannwart and M. M. Ganzarolli (2015). Numerical and experimental study of an axially induced swirling pipe flow, *International Journal of Heat and Fluid Flow* 53,81-90.
- Safikhani, S. A. (2020). The effect of magnetic field on the performance of new design cyclone separators, *Advanced Powder Technology* 31, 2541-2554.
- Souza, R., V. Salvo and D. A. M. Martins (2012). Large Eddy Simulation of the gas-particle flow in cyclone separators, *Separation and Purification Technology* 94, 61-70.
- Souza, R., V. Salvo and D. M. Martins (2015). Simulation of the performance of small cyclone separators through the use of Post Cyclones (PoC) and annular overflow ducts, *Separation and Purification Technology* 142, 71-82.
- Sun, J. Y. Y. (2018). Multi-objective optimization of a gas cyclone separator using genetic algorithm and computational fluid dynamics, *Powder Technology* 325, 347-360.
- Sun, S. K., S. D. Yang, H. S. Kim and J. Y. Yoon (2017). Multi-objective optimization of a Stairmand cyclone separator using response surface methodology and computational fluid dynamics, *Powder Technology* 320, 51-65.
- Tag, G. D. and J. Yanik (2018). Influences of feedstock type and process variables on hydrochar properties, *Bioresource Technology* 250, 337-344.
- Venkatesh, R., S. Kumar, S. P. Sivapirakasam, M. Sakthivel, D. Venkatesh and S. Y. Arafath (2020). Multi-objective optimization, experimental and CFD approach for performance analysis in square cyclone separator, *Powder Technology* 371, 115-129.
- Venkatesh, S. P. Sivapirakasam, M. Sakthivel, S. Ganeshkumar, M. M. Prabhu and M. Naveenkumar (2021). Experimental and numerical investigation in the series arrangement square cyclone separator, *Powder Technology* 383, 93-103.
- Wei, G. S. and C. Gao (2020). Numerical analysis of axial gas flow in cyclone separators with different vortex finder diameters and inlet dimensions, *Powder Technology* 369, 321-333.
- Wu, X. W. and Y. Zhou (2018). Experimental study and numerical simulation of the characteristics of a percussive gas-solid separator, *Particuology* 36, 96-105.
- Xing, W. P., Q. Zhang, Y. Yang and D. Han (2021). The multi-objective optimization of an axial cyclone separator in the gas turbine, *International Journal of Energy Research* 46, 3428-3442.
- Yang, J. Wang, X. Sun and M. Xu (2019). Multi-objective optimization design of spiral demister with punched holes by combining response surface method and genetic algorithm, *Powder Technology* 355, 106-118.
- Zhao, B. L. and Y. Zhong (2013). Euler-Euler modeling of a gas-solid bubbling fluidized bed with kinetic theory of rough particles, *Chemical Engineering Science* 104, 767-779.
- Zhao, Y. S. (2010). Artificial neural network-based modeling of pressure drop coefficient for cyclone separators, *Chemical Engineering Research and Design* 88, 606-613.
- Zhou, Z. H., Q. Zhang, Q. Wang and X. Lv (2019). Numerical study on gas-solid flow characteristics of ultra-light particles in a cyclone separator, *Powder Technology* 344, 784-796.